Berry Curvature of Low-Energy Excitons in Rhombohedral Graphene

Henry Davenport, Frank Schindler, and Johannes Knolle^{2,3,1}

¹Blackett Laboratory, Imperial College London, London SW7 2AZ, United Kingdom
²Technical University of Munich, TUM School of Natural Sciences, Physics Department, 85748 Garching, Germany
³Munich Center for Quantum Science and Technology (MCQST), Schellingstr. 4, 80799 München, Germany

We investigate low energy excitons in rhombohedral pentalayer graphene encapsulated by hexagonal boron nitride (hBN/R5G/hBN), focusing on the regime at the experimental twist angle $\theta=0.77^{\circ}$ and with an applied electric field. We introduce a new low-energy two-band model of rhombohedral graphene that captures the band structure more accurately than previous models while keeping the number of parameters low. Using this model, we show that the centres of the exciton Wannier functions are displaced from the moiré unit cell origin by a quantised amount – they are instead localised at C_3 -symmetric points on the boundary. We also find that the exciton shift is electrically tunable: by varying the electric field strength, the exciton Wannier centre can be exchanged between inequivalent corners of the moiré unit cell. Our results suggest the possibility of detecting excitonic corner or edge modes, as well as novel excitonic crystal defect responses in hBN/R5G/hBN. Lastly, we find that the excitons in hBN/R5G/hBN inherit excitonic Berry curvature from the underlying electronic bands, enriching their semiclassical transport properties. Our results position rhombohedral graphene as a compelling tunable platform for probing exciton topology in moiré materials.

I. INTRODUCTION

The study of Berry curvature effects has played a central role in advancing our understanding of non-interacting electrons in condensed matter systems [1]. More recently, there has been growing interest in extending this framework to interacting systems. Efforts in this direction include the topological classification of ground states in the presence of interactions [2–5], as well as the investigation of Berry curvature effects and the topological classification of interaction-induced excitations, such as excitons [6–11].

Rhombohedral graphene has emerged as a compelling platform for studying non-trivial ground-state topology induced by interactions. Experiments have found that rhombohedral graphene exhibits both the integer and fractional quantum Hall effects [12] and a comprehensive theoretical understanding of these phenomena remains an area of active research [13–18]. In this work, we take an alternative approach and focus on the excitations rather than the ground state, specifically the excitons at charge neutrality. We study rhombohedral pentalayer graphene (R5G) encapsulated by hexagonal boron nitride (hBN), shown in Fig. 1a. When an electric field is applied we can obtain two well-gapped electronic bands around the Fermi level at charge neutrality [13]. Since the bands immediately above and below the Fermi energy are layer polarised, the twist angle of the hBN either side of the R5G strongly influences the topology and dispersion of these electronic bands. The electronic bands are therefore highly tunable making hBN/R5G/hBN an ideal testbed for studying the topology of low energy excitons emerging from topological electron bands.

In this paper we show that, at the experimentally relevant twist angle $\theta = 0.77^{\circ}$ [12], the exciton Wannier states are shifted to the edge of the moiré unit cell and their Wannier centre depends on the electronic potential applied across the rhombohedral graphene layers.

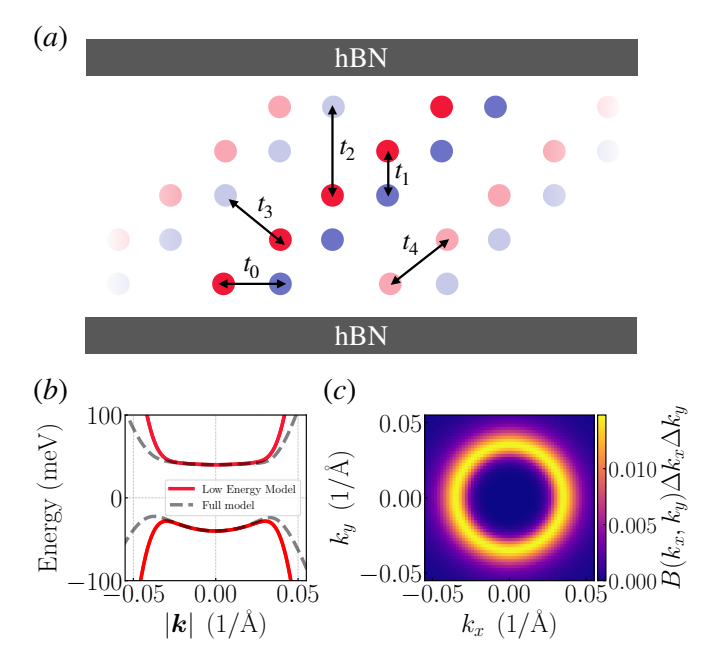


FIG. 1. Rhombohedral graphene encapsulated between two hBN layers. The hopping parameters of our tight-binding model are labelled $t_{0...4}$ in (a). The A sublattice of graphene is shown in red and the B sublattice in blue. (b) Dispersions of the low energy model and the full model of the free-standing rhombohedral graphene (with displacement field $u_D=20 {\rm meV}$). (c) The Berry curvature $[B(k_x,k_y)]$ distribution of the low energy model.

They are therefore analogous to obstructed atomic insulators in non-interacting electron systems [19]. We note however that this shift is inherited from the electronic bands and so is not like the shift excitons described in Ref. 6 where the excitons have maximally localised exciton Wannier centres [20, 21] shifted with respect to the electronic Wannier centres. Despite this, we expect that rhombohedral graphene still exhibits novel 'excitonic' de-

fect and edge responses. We also find that the Berry curvature of the excitons can be tuned using the applied electric field, allowing for an experimental exploration of the role of Berry curvature on excitonic properties. Given these attributes, rhombohedral graphene presents a unique system to explore the effects of exciton Berry curvature on exciton transport properties, both experimentally and theoretically.

This paper is structured as follows. We begin by outlining the non-interacting physics underlying the band dispersion and Berry curvature distribution. In Sec. II we introduce a new simple low-energy 2 band model of rhombohedral graphene that better captures the dispersion shape around the Dirac point compared to the wellstudied k^5 model [18]. In addition, we show how the moiré potential modifies the dispersion and band topology. In Sec. III we detail our methodology for calculating the exciton dispersion and exciton Berry curvature. Our findings indicate that the applied electric field can be used to tune the lowest-energy excitons to regimes where the exciton Berry curvature is enhanced. We predict that this could lead to a measurable thermal Hall effect [22]. Additionally, we identify regimes where the exciton Wannier centres are obstructed from the centre of the moiré unit cell, with the Wyckoff position they are centred at tunable using the applied electric field. In Sec. IV we discuss the experimental consequences of this exciton shift in terms of defect responses detectable using Electron Energy Loss Spectroscopy (EELS) [23, 24].

II. BAND STRUCTURE

We first derive an economical model that captures the band structure of R5G as well as that of hBN/R5G/hBN with a moiré twist.

A. Low energy model

We begin by formulating a new low-energy effective model for isolated pentalayer rhombohedral graphene, which serves as the basis for all subsequent analysis. Our starting point is the full 10-band tight-binding model previously studied in Ref. 14, with interlayer and intralayer hopping parameters as illustrated in Fig. 1 (see Appendix A for a full description). This model includes an external perpendicular electric field - known as the displacement field. To model this we add a layer-dependent onsite potential, where the potential difference between adjacent layers is uniform and denoted by u_D [14].

When u_D is non-zero, and for momenta near the Dirac point, the electronic wave functions associated with the conduction and valence bands closest to the Fermi level become strongly localised on sublattice A of layer 1 and sublattice B of layer 5 [14]. This layer polarization enables a projection onto the corresponding subspace, yielding a reduced two-band model that captures the low-

energy physics at charge neutrality (see Appendix A for detailed derivations). With our method we can systematically include higher order corrections beyond the simpler two band models studied previously [18]. In particular we incorporate a key correction absent from previous work: namely, the intrinsic quadratic dispersion that dominates at small momenta \boldsymbol{k} near the Dirac point [see Fig. 1 panel (b)]. We show that this curvature can be systematically retained within the effective theory by including a correction quadratic in the momentum. This results in the following two-band Hamiltonian that more accurately reflects the low-energy behaviour of rhombohedral graphene,

$$h_{\text{eff}}(\mathbf{k}) = \begin{cases} 2u_D + \gamma_-(k_x^2 + k_y^2) & \frac{v_F^5}{t_1^4} (k_x - ik_y)^5 \\ \frac{v_F^5}{t_1^4} (k_x + ik_y)^5 & -2u_D + \gamma_+(k_x^2 + k_y^2) \end{cases}, \tag{1}$$

where $v_F = \frac{\sqrt{3}}{2}t_0a$ and a is the graphene lattice constant. The numerical values of the hoppings are given in Appendix A [14, 25]. The γ_{\pm} take a simple form if we assume small u_D (specifically $u_D \ll t_3 \ll t_0$) and expand to first order in u_D ,

$$\gamma_{\pm} \approx \frac{2v_F v_4}{t_1} \pm \frac{u_D v_F^2}{t_1^2},$$
(2)

where $v_4 = \frac{\sqrt{3}}{2}t_4a$. This simplified model predicts a sign change in the curvature of the higher-energy band at the Dirac point when the displacement field reaches $u_D = \frac{2v_4t_1}{v_F} \sim 35$ meV. In contrast, the curvature of the lower-energy band at the Dirac point remains unchanged for all $u_D \geq 0$. This sign change is absent in the model presented in Ref. [18], which neglects this diagonal quadratic correction.

Fig. 1b compares the band dispersions of the full and simplified models for a representative set of parameters. As expected, both models closely agree near the Dirac point, with increasing deviations at larger momenta. In addition to capturing the band dispersion, the simplified model also reproduces the Berry curvature distribution of the full model [18]. As shown in Fig. 1c, the Berry curvature in the simplified model is concentrated in a ring around the Dirac point. This ring occurs at the momenta where the band dispersion transitions from being nearly flat to rapidly increasing or decreasing.

B. Moiré Hamiltonian

We investigate pentalayer rhombohedral graphene (R5G) encapsulated between two layers of hexagonal boron nitride (hBN), as illustrated in Fig. 1. In contrast to most previous work, which has considered coupling of the R5G to hBN on only one side [13, 14, 17], we assume that both the top and bottom hBN layers couple equally to the R5G (as also studied in Ref. [13]).

Due to the lattice parameter mismatch between hBN and graphene, a moiré pattern forms which folds the bands into the mini BZ (mBZ) (shown in Fig. 2a). The (real space) unit cell is enlarged compared to the isolated R5G unit cell (Fig. 2b). The moiré unit cell has a periodicity $(a_{\text{moir\'e}} = |L_{1/2}| \text{ in Fig. 2b})$ which depends on the relative twist angle θ between the primitive lattice vectors of the hBN and R5G and the lattice constant missmatch between graphene and hBN [25]. We study the regime where both the top and bottom hBN layers are aligned at the same angle relative to the graphene, thereby avoiding the formation of a super-moiré pattern. The hBN layers are modelled as an effective potential acting on the outermost layers of the rhombohedral graphene [25]. Here we summarise the method used to model the moiré system. see Appendix B for the full details. Since our effective Hamiltonian retains only the A sublattice in the bottom layer and the B sublattice in the top layer, we apply the moiré potential exclusively to these sites. For layer l we use, [25]

$$V_{\text{eff}}^{l}(\mathbf{r}) = V_0 + V_1 \sum_{\substack{\eta \in \{1, -1\}\\ j \in \{1, 2, 3\}}} \exp\left[i\eta \left(\mathbf{g}_j \cdot \mathbf{r} + \psi_{\xi} + \phi_l\right)\right].$$
(3)

Here, the sum runs over moiré reciprocal lattice vectors g_j , using the "first harmonic" approximation where we retain only the first shell of reciprocal vectors surrounding the first moiré Brillouin zone [13, 25]. There is a phase shift ψ_{ξ} which depends on the stacking configuration, for example, the A sublattice of graphene may lie above either a boron atom ($\xi=0$) or a nitrogen atom ($\xi=1$), and this leads to differing phases for the effective potential [25]. We restrict our study to $\xi=0$ stacking for both the top and bottom layers (for which $\psi_{\xi}=223.5^{\circ}$) [25]. The layer dependent phase factor is only nonzero on the top layer, $\phi_l=\frac{2\pi N_l}{3}\delta_{l,4}$ [13]. This phase accounts for the relative shift in the moiré potential between the A sublattice on the bottom later and the B sublattice on the top layer [13].

We define the fermionic creation operators, $c_{\mathbf{k},\mathbf{Q},l}^{\dagger} = c_{\mathbf{k}+\mathbf{Q},l}^{\dagger}$ where the momentum \mathbf{k} is in the mBZ, \mathbf{Q} are the moiré reciprocal lattice vectors, and l is the layer index. The total moiré Hamiltonian is.

$$H_{M} = H_{0} + H_{V} = \sum_{\boldsymbol{k} \in \text{mBZ}} \sum_{\boldsymbol{Q}, \boldsymbol{Q}'} \sum_{l,l'} h_{(\boldsymbol{Q},l),(\boldsymbol{Q}',l')}^{(m)}(\boldsymbol{k}) c_{\boldsymbol{k},\boldsymbol{Q},l}^{\dagger} c_{\boldsymbol{k},\boldsymbol{Q}',l'}, \quad (4)$$

where,

$$h_{(\mathbf{Q},l),(\mathbf{Q}',l')}^{(m)}(\mathbf{k}) = \{ [h_{\text{eff}}(\mathbf{k} + \mathbf{Q})]_{l,l'} + V_0 \delta_{l,l'} \} \, \delta_{\mathbf{Q},\mathbf{Q}'} + V_1 \sum_{\substack{\eta \in \{1,-1\}\\j \in \{1,2,3\}}} \delta_{\mathbf{Q},\mathbf{Q}'-\eta \mathbf{g}_j}.$$
(5)

Here the first term $h_{\text{eff}}(\mathbf{k})$ represents the original low energy rhombohedral graphene model without the moiré

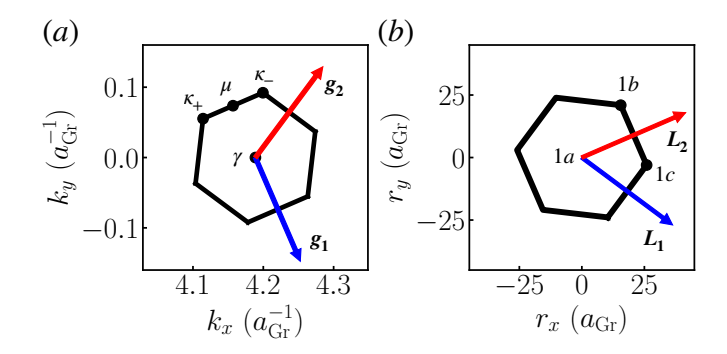


FIG. 2. The mini Brillouin zone (a) and unit cell (b) for hBN/R5G/hBN with twist angle $\theta=0.77^{\circ}$. The moiré reciprocal lattice vectors are labelled $\mathbf{g_1}$, $\mathbf{g_2}$, and the high symmetry points are γ , κ_+ , κ_- and μ . The real space unit cell [panel (b)] shows the lattice vectors $\mathbf{L_1}$, $\mathbf{L_2}$ and maximal Wyckoff positions 1a, 1b, 1c.

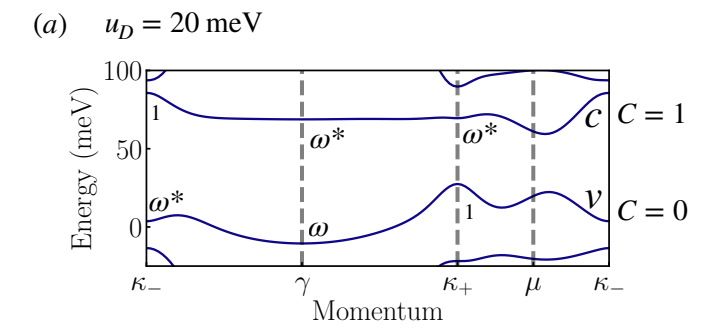
coupling. The moiré system retains C_3 symmetry and as shown in Fig. 2 there are three high symmetry points γ , κ_+ and κ_- . To obtain a finite matrix size, we truncate the set of \boldsymbol{Q} vectors in the moiré Hamiltonian to those within a ring around the γ point with $|\boldsymbol{Q}| \leq 5[2\pi \cdot (a_{\text{moiré}})^{-1}]$.

C. Non-interacting band structure

Using the model outlined above, we calculate the electronic dispersion of the hBN/R5G/hBN stack. Examples of the non-interacting band structures for $\theta=0.77^\circ$ and $u_D=\pm 20$ meV are shown in Fig. 3. The hBN layers fold the bands of isolated rhombohedral graphene into the moiré Brillouin zone (mBZ) and hybridize the folded bands, resulting in two gapped bands immediately above (labeled c) and below the Fermi level (labeled v) at charge neutrality. The hBN moiré potential preserves C_3 symmetry, allowing us to use symmetry indicators to compute the Chern number (mod 3) of the electronic bands. The C_3 eigenvalues can take the values 1, ω , or ω^* , where $\omega=e^{i\frac{2\pi}{3}}$. The Chern number C is related to the product of the C_3 eigenvalues ($\lambda_k^{C_3}$) at the high-symmetry points as follows: [26]

$$e^{i2\pi C} = \prod_{k \in \{\gamma, \kappa_+, \kappa_-\}} \lambda_k^{C_3}.$$
 (6)

For $u_D=20$ meV, we find that the empty (conduction) band has a Chern number of 1, while the occupied (valence) band has a Chern number of 0. For $u_D=-20$ meV, both bands have Chern number 0. The complete phase diagram of Chern number as a function of displacement field u_D and twist angle θ , reveals a variety of possible Chern numbers for both bands, even within this simple model of R5G (see Appendix C for more details). Figure 4 shows the Berry curvature of the non-interacting bands for the chosen parameters, revealing that it is concentrated at the edges of the mBZ. At



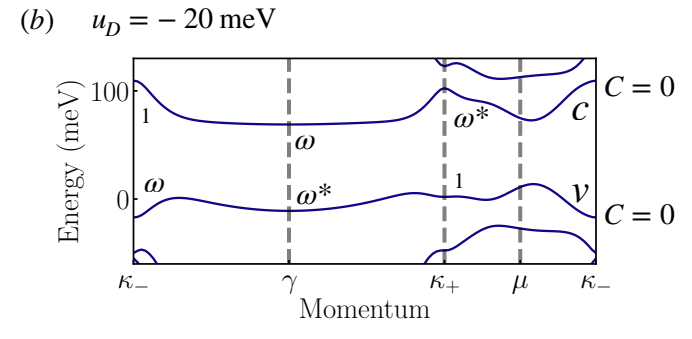


FIG. 3. Electronic (non-interacting) dispersion at $\theta = 0.77^{\circ}$ for displacement field $u_D = 20 \,\mathrm{meV}$ and $u_D = -20 \,\mathrm{meV}$. The C_3 symmetry eigenvalues are shown at the high symmetry points in terms of $\omega = \exp(i2\pi/3)$.

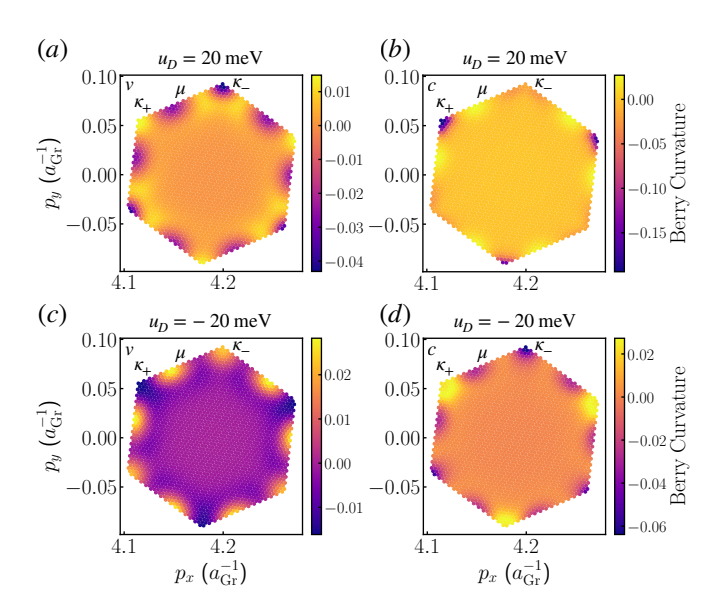


FIG. 4. Electronic Berry curvature for the occupied (v) and empty band (c). For parameters $\theta = 0.77^{\circ}$ and $u_D = \pm 20 \text{ meV}$.

 $u_D=20~\mathrm{meV}$ the maxima and minima of the bands are also at the edge of the mBZ, indicating that low-energy charge-neutral excitations are dominated by states near the mBZ edges. We therefore expect this large electronic Berry curvature to also be visible in the exciton Berry curvature.

III. EXCITONS

We next study the exciton bound states of hBN/R5G/hBN, their dispersion and Berry curvature.

A. Methods

We calculate the exciton dispersion and wave functions in hBN/R5G/hBN stacks that form from the two well separated bands shown Fig. 3. At charge neutrality the ground state has the lower band (v) occupied and the upper band (c) unoccupied. We will consider excitons formed from these two bands where $c_{k,c}$ $(c_{k,v})$ annihilates an electron in the conduction (valence) band at crystal momentum k. We restrict our calculation to just these two bands since we are interested in the low energy spectrum which will not be effected significantly by the inclusion of higher and lower energy bands. The wave function of an exciton at momentum p is expressed as:

$$|\psi^{\mathbf{p}}\rangle = \sum_{\mathbf{k}\in\text{mBZ}} \phi_{\mathbf{k}}^{\mathbf{p}} c_{\mathbf{p}+\mathbf{k},c}^{\dagger} c_{\mathbf{k},v} |\text{GS}\rangle,$$
 (7)

where $|\text{GS}\rangle$ denotes the non-interacting ground state, projected onto the two bands of interest (e.g., $|\text{GS}\rangle = \prod_{k} c_{k,v}^{\dagger} |0\rangle$). We study the spin-valley polarized regime and so we restrict our focus to excitons at just one valley and a single spin species [14].

To model the excitons we project both the kinetic and interaction Hamiltonians into the basis $c_{p+k,c}^{\dagger}c_{k,v}|\text{GS}\rangle$ [27, 28]. The resulting exciton Hamiltonian, detailed in Appendix D, is written in terms of non-interacting single-particle energies and the products of the non-interacting electronic wave functions (the "form factors"). These products are given by:

$$U_{\alpha,\alpha',\beta,\beta'}^{\boldsymbol{p},\boldsymbol{k},\boldsymbol{k}'} = \sum_{\boldsymbol{Q}} V(\boldsymbol{p} + \boldsymbol{Q}) \left\langle u_{\boldsymbol{p}+\boldsymbol{k}+\boldsymbol{Q}}^{\alpha} | u_{\boldsymbol{p}'}^{\alpha'} \right\rangle \left\langle u_{\boldsymbol{p}'}^{\beta} | u_{\boldsymbol{p}+\boldsymbol{k}'+\boldsymbol{Q}}^{\beta'} \right\rangle,$$
(8)

where $|u_{\mathbf{p}}^{\alpha}\rangle$ represents the eigenvector of the moiré Hamiltonian [Eq. (5)] for momentum \mathbf{p} and band α . We use the double-gated Coulomb potential, which accounts for the screening effects introduced by the metal electrodes either side of the sample. This potential is given by,

$$V(|\mathbf{p}|) = \frac{V_0 \tanh(|\mathbf{p}|d)}{|\mathbf{p}|},\tag{9}$$

where d is the metal electrode gate distance. We use d=250 Å [14] for the following calculations. The interaction strength $V_0 = \frac{2\pi}{\epsilon_0 \epsilon_r}$ depends on the relative permittivity ϵ_r , we use $\epsilon_r = 6$ [16]. We calculate the exciton Berry curvature using the gauge invariant method of Ref. 21 and 29 (see Appendix F for details).

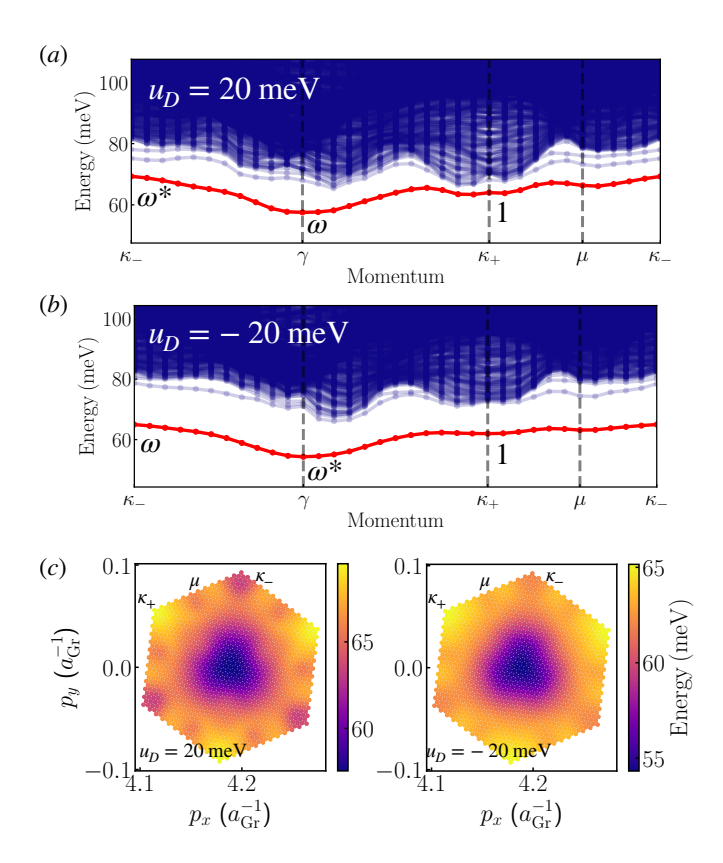


FIG. 5. Exciton dispersion (in red) with particle-hole continuum above (in blue) for $\theta=0.77^{\circ}$ (a) $u_D=20$ meV and (b) $u_D=-20$ meV. In both cases the C_3 symmetry eigenvalues of the excitons are marked. The dispersion of the excitons throughout the whole BZ for both parameter choices is shown in (c).

| u_D | $\lambda_{\gamma}^{\mathrm{exc}}$ | $\lambda_{\kappa_{+}}^{\mathrm{ex}}$ | $^{\mathrm{c}}\lambda_{\kappa_{-}}^{\mathrm{exc}}$ | $oldsymbol{s}_{	ext{exc}}$ |
|----------|-----------------------------------|--------------------------------------|----------------------------------------------------|----------------------------|
| 20 meV | ω | 1 | ω^* | 1c |
| -20 meV | ω^* | 1 | ω | 1b |

TABLE I. C_3 eigenvalues of the exciton wave function at high-symmetry points in the Brillouin zone for two different parameter choices. The exciton Wannier centre s_{exc} is stated in terms of the Wyckoff positions (see Fig. 2b).

B. Exciton dispersion and Berry curvature

Fig. 5 shows the exciton dispersions at a twist angle of $\theta=0.77^{\circ}$ under a displacement field of $u_D=20~{\rm meV}$ and $u_D=-20~{\rm meV}$. For both parameter choices, the exciton binding energy is largest around the γ point since the interaction potential V(p) peaks at p=0. The excitons in both cases are fully gapped across the mBZ but the maximum binding energy for $u_D=-20~{\rm meV}$ is substantially larger at $\sim 17~{\rm meV}$ compared to $\sim 11~{\rm meV}$ for $u_D=20~{\rm meV}$. We can use symmetry indicators to study the exciton band topology. We compute the total C_3 eigenvalues of the many body exciton wave function at the high-symmetry points in the Brillouin zone (see Fig. 5). In both parameter regimes the exciton Chern

number of the band is 0. However, despite the trivial Chern number, there is interesting crystalline topology. The symmetry indicators of the excitons can be used to calculate the centre of the maximally localised exciton Wannier states for the exciton band [6, 20, 21]. In Tab. I we show the shift of the maximally localised exciton Wannier function from the centre of the moiré unit cell $s_{\rm exc}$ (see Appendix E for details of this calculation). In both cases, the exciton Wannier centre is not at the centre of the moiré unit cell. In addition, the exciton Wannier centre varies between the two configurations: at $u_D = 20\,\mathrm{meV}$ it sits at the 1c Wyckoff position but for $u_D = -20\,\mathrm{meV}$ it is at the 1b Wyckoff positions.

Beyond the global topology of the exciton band, the exciton Berry curvature (Fig. 6) reveals marked differences between the two displacement field values. For $u_D = 20 \text{ meV}$, the curvature exhibits pronounced minima and maxima, despite the total Chern number of the exciton band being zero. These features originate from the underlying *electronic* Berry curvature. Specifically, the enhanced exciton Berry curvature near the γ point can be seen to be inherited from the *electronic* Berry curvature. In Fig. 3a we can see that the lowest energy particle hole excitations take an electron from the κ_{+} point in the lower band to μ in the upper band. Since the electronic Berry curvature is strongly concentrated at κ_{+} (Fig. 4a), excitons with momentum $p \approx \mu - \kappa_{+}$ (or C_3 rotations of this momentum) inherit this curvature. In contrast, for $u_D = -20 \text{ meV}$, the exciton Berry curvature is nearly uniform and vanishing (Fig. 6b). This occurs because the electronic bands do not have as pronounced maxima at the edge of the mBZ compared to the $u_D = 20 \text{ meV}$ case. Therefore the exciton bands are mainly composed of electronic states from the centre of the mBZ. The Berry curvature of the electronic bands at the centre can be seen to be very close to 0 (see Fig. 4c and 4d) and so the exciton Berry curvature is similarly small in magnitude.

Excitons will thermally occupy the exciton band leading to an enhanced population at the band minimum. Therefore, whilst the overall exciton band is topologically trivial, the locally enhanced Berry curvature in the vicinity of the band minimum (at $u_D = 20 \text{ meV}$) will influence exciton transport behaviour. The exciton Berry curvature, integrated over circular regions of increasing radius centred at γ , is shown in Fig. 6c. Due to the presence of both minima and maxima in the Berry curvature, the integrated value oscillates with distance from γ in the Brillouin zone for $u_D = 20 \text{ meV}$. This will lead to a temperature dependence of response functions sensitive to the exciton Berry curvature, as thermal excitation allows excitons to occupy states beyond the band minimum, altering the Boltzmann-weighted Berry curvature. In contrast the flat exciton Berry of the $u_D = -20 \text{ meV}$ will not have such oscillatory exciton Berry curvature effects. Hence, rhombohedral graphene provides a platform in which it is possible to electrically tune between regimes with and without *excitonic* Berry curvature effects.

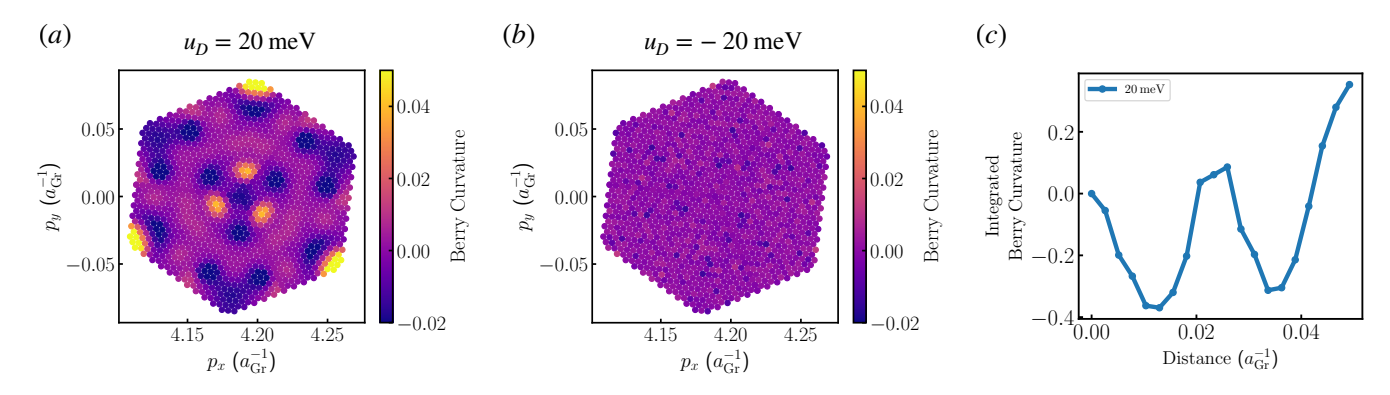


FIG. 6. Exciton Berry curvature for the lowest energy exciton band for $\theta = 0.77^{\circ}$, $(a): u_D = 20 \text{ meV}$ and $(b): u_D = -20 \text{ meV}$. Panel (c) is the exciton Berry curvature integrated over circles of increasing radius centred at the γ point for $u_D = 20 \text{ meV}$ (not shown for full mBZ).

IV. DISCUSSION

The response and transport properties of electrons in non-interacting bands are well known to be influenced by the electronic Berry curvature [1]. Fully elucidating the transport effects of exciton Berry curvature represents a new frontier in the study of quantum transport phenomena. Our work implies that rhombohedral graphene is a possibly important material for exploring the interplay of excitons and topology. For $u_D = -20 \text{ meV}$, the Berry curvature of the single electron dispersion of rhombohedral graphene is concentrated at the edge of the mBZ, exactly where the low energy excitons are formed, meaning that the lowest energy excitons in rhombohedral graphene inherit the Berry curvature of the electronic bands. The transport properties of excitons are likely to be influenced by this exciton Berry curvature. One possible measurable consequence of the enhanced Berry curvature at a displacement field of $u_D = 20 \text{ meV}$ is a thermal Hall effect [22]. Applying an in-plane temperature gradient to the sample would generate a transverse exciton current, i.e. most clearly visible as a chiral exciton current at the edge of the system. Typically such exciton currents are hard to measure because excitons are neutral, however, as we have seen, the conduction band and valence band electronic wave functions are layer polarised. Hence, the exciton flow could be detected by measuring the electron or hole current on either the top or bottom layer of the sample similar to a drag current [30, 31].

We have also predicted that the maximally localised exciton Wannier states are shifted away from the centre of the unit cell, directly analogous to the concept of an obstructed atomic insulator in non-interacting electron systems [19]. Obstructed atomic insulators are known

to possess crystal defect responses that depend on the Wannier state shift, as well as corner or edge polarization [32]. Hence we expect that the exciton Wannier state shift in rhombohedral graphene could analogously lead to new excitonic crystal defect responses and exciton corner or edge modes [6]. The current spatial resolution of exciton probes would not allow it to be possible to detect these effects in bare graphene with a unit cell of order 2.46 Å, but the enhanced moiré unit cell size increases the shift to within the resolution range of techniques like EELs, which can achieve spatial resolutions on the order of \sim nm [23, 24]. Moiré systems such as hBN/R5G/hBN therefore offer a promising platform for experimentally probing exciton crystalline topology. However, understanding the full range of experimental signatures, beyond edge states [6], remains a compelling and open direction for future research.

ACKNOWLEDGMENTS

We would like to thank Johannes Lischner for useful discussions. We acknowledge support from the Imperial-TUM flagship partnership. This work was supported by a UKRI Future Leaders Fellowship MR/Y017331/1. HD acknowledges support from the Engineering and Physical Sciences Research Council (grant number EP/W524323/1). JK acknowledges support from the Deutsche Forschungsgemeinschaft (DFG, German Research Foundation) under Germany's Excellence Strategy–EXC–2111–390814868, DFG grants No. KN1254/1-2, KN1254/2-1, and TRR 360 - 492547816; as well as the Munich Quantum Valley, which is supported by the Bavarian state government with funds from the Hightech Agenda Bayern Plus.

^[1] D. Xiao, M.-C. Chang, and Q. Niu, Berry phase effects on electronic properties, Rev. Mod. Phys. 82, 1959 (2010).

^[2] M. O. Soldini, N. Astrakhantsev, M. Iraola, A. Tiwari, M. H. Fischer, R. Valentí, M. G. Vergniory, G. Wagner,

- and T. Neupert, Interacting topological quantum chemistry of mott atomic limits, Phys. Rev. B **107**, 245145 (2023).
- [3] K. Shiozaki, C. Z. Xiong, and K. Gomi, Generalized homology and atiyah-hirzebruch spectral sequence in crystalline symmetry protected topological phenomena, Progress of Theoretical and Experimental Physics 2023, 083I01 (2023), https://academic.oup.com/ptep/articlepdf/2023/8/083I01/51118278/ptad086.pdf.
- [4] N. Manjunath, V. Calvera, and M. Barkeshli, Characterization and classification of interacting (2 + 1)-dimensional topological crystalline insulators with orientation-preserving wallpaper groups, Phys. Rev. B 109, 035168 (2024).
- [5] J. Herzog-Arbeitman, B. A. Bernevig, and Z.-D. Song, Interacting topological quantum chemistry in 2d with many-body real space invariants, Nature Communications 15, 1171 (2024).
- [6] H. Davenport, J. Knolle, and F. Schindler, Interactioninduced crystalline topology of excitons, Physical Review Letters 133, 10.1103/physrevlett.133.176601 (2024).
- [7] Y. H. Kwan, Y. Hu, S. H. Simon, and S. A. Parameswaran, Exciton band topology in spontaneous quantum anomalous hall insulators: Applications to twisted bilayer graphene, Phys. Rev. Lett. 126, 137601 (2021).
- [8] P. Froese, T. Neupert, and G. Wagner, Topological excitons in moiré mote₂/wse₂ heterobilayers, Phys. Rev. Res. 7, 023047 (2025).
- [9] W. Yao and Q. Niu, Berry phase effect on the exciton transport and on the exciton bose-einstein condensate, Phys. Rev. Lett. 101, 106401 (2008).
- [10] W. J. Jankowski, J. J. P. Thompson, B. Monserrat, and R.-J. Slager, Excitonic topology and quantum geometry in organic semiconductors, Nature Communications 16, 4661 (2025).
- [11] H.-Y. Xie, P. Ghaemi, M. Mitrano, and B. Uchoa, Theory of topological exciton insulators and condensates in flat chern bands, Proceedings of the National Academy of Sciences 121, e2401644121 (2024), https://www.pnas.org/doi/pdf/10.1073/pnas.2401644121
- [12] Z. Lu, T. Han, Y. Yao, A. P. Reddy, J. Yang, J. Seo, K. Watanabe, T. Taniguchi, L. Fu, and L. Ju, Fractional quantum anomalous hall effect in a graphene moire superlattice (2023), arXiv:2309.17436 [cond-mat.mes-hall].
- [13] J. Herzog-Arbeitman, Y. Wang, J. Liu, P. M. Tam, Z. Qi, Y. Jia, D. K. Efetov, O. Vafek, N. Regnault, H. Weng, Q. Wu, B. A. Bernevig, and J. Yu, Moiré fractional chern insulators. ii. first-principles calculations and continuum models of rhombohedral graphene superlattices, Phys. Rev. B 109, 205122 (2024).
- [14] J. Dong, T. Wang, T. Wang, T. Soejima, M. P. Zaletel, A. Vishwanath, and D. E. Parker, Anomalous hall crystals in rhombohedral multilayer graphene. i. interactiondriven chern bands and fractional quantum hall states at zero magnetic field, Phys. Rev. Lett. 133, 206503 (2024).
- [15] T. Soejima, J. Dong, T. Wang, T. Wang, M. P. Zaletel, A. Vishwanath, and D. E. Parker, Anomalous hall crystals in rhombohedral multilayer graphene. ii. general mechanism and a minimal model, Phys. Rev. B 110, 205124 (2024).
- [16] B. A. Bernevig and Y. H. Kwan, "berry trashcan" model of interacting electrons in rhombohedral graphene (2025), arXiv:2503.09692 [cond-mat.str-el].

- [17] J. Yu, J. Herzog-Arbeitman, Y. H. Kwan, N. Regnault, and B. A. Bernevig, Moiré fractional chern insulators iv: Fluctuation-driven collapse of fcis in multi-band exact diagonalization calculations on rhombohedral graphene (2024), arXiv:2407.13770 [cond-mat.str-el].
- [18] Z. Dong, A. S. Patri, and T. Senthil, Stability of anomalous hall crystals in multilayer rhombohedral graphene, Physical Review B 110, 10.1103/physrevb.110.205130 (2024).
- [19] B. Bradlyn, L. Elcoro, J. Cano, M. G. Vergniory, Z. Wang, C. Felser, M. I. Aroyo, and B. A. Bernevig, Topological quantum chemistry, Nature 547, 298 (2017).
- [20] J. B. Haber, D. Y. Qiu, F. H. da Jornada, and J. B. Neaton, Maximally localized exciton wannier functions for solids, Phys. Rev. B 108, 125118 (2023).
- [21] H. Davenport, J. Knolle, and F. Schindler, Exciton berryology (2025), arXiv:2507.22983 [cond-mat.mes-hall].
- [22] X.-T. Zhang, Y. H. Gao, and G. Chen, Thermal hall effects in quantum magnets, Physics Reports 1070, 1 (2024).
- [23] H. C. Nerl, K. T. Winther, F. S. Hage, K. S. Thygesen, L. Houben, C. Backes, J. N. Coleman, Q. M. Ramasse, and V. Nicolosi, Probing the local nature of excitons and plasmons in few-layer mos2, npj 2D Materials and Applications 1, 2 (2017).
- [24] S. Susarla, M. H. Naik, D. D. Blach, J. Zipfel, T. Taniguchi, K. Watanabe, L. Huang, R. Ramesh, F. H. da Jornada, S. G. Louie, P. Ercius, and A. Raja, Hyperspectral imaging of exciton confinement within a moiré unit cell with a subnanometer electron probe, Science 378, 1235–1239 (2022).
- [25] P. Moon and M. Koshino, Electronic properties of graphene/hexagonal-boron-nitride moiré superlattice, Phys. Rev. B 90, 155406 (2014).
- [26] C. Fang, M. J. Gilbert, and B. A. Bernevig, Bulk topological invariants in noninteracting point group symmetric insulators, Phys. Rev. B 86, 115112 (2012).
- [27] F. Schindler, O. Vafek, and B. A. Bernevig, Trions in twisted bilayer graphene, Phys. Rev. B 105, 155135 (2022).
- [28] E. Khalaf and A. Vishwanath, Baby skyrmions in chern ferromagnets and topological mechanism for spin-polaron formation in twisted bilayer graphene, Nature Communications 13, 6245 (2022).
- [29] T. Fukui, Y. Hatsugai, and H. Suzuki, Chern numbers in discretized brillouin zone: Efficient method of computing (spin) hall conductances, Journal of the Physical Society of Japan 74, 1674–1677 (2005).
- [30] P. Nguyen, L. Ma, R. Chaturvedi, K. Watanabe, T. Taniguchi, J. Shan, and K. Mak, Perfect coulomb drag in a dipolar excitonic insulator (2023), arXiv preprint arXiv:2309.14940.
- [31] R. Qi, A. Y. Joe, Z. Zhang, J. Xie, Q. Feng, Z. Lu, Z. Wang, T. Taniguchi, K. Watanabe, S. Tongay, et al., Perfect coulomb drag and exciton transport in an excitonic insulator, Science 388, 278 (2025).
- [32] F. Schindler, S. S. Tsirkin, T. Neupert, B. Andrei Bernevig, and B. J. Wieder, Topological zero-dimensional defect and flux states in three-dimensional insulators, Nature Communications 13, 5791 (2022).
- [33] F. Zhang, B. Sahu, H. Min, and A. H. MacDonald, Band structure of abc-stacked graphene trilayers, Phys. Rev. B 82, 035409 (2010).

Appendix A: Pentalayer rhombohedral graphene

We derive the low energy model for pentalayer rhombohedral graphene (R5G) introduced in the main text. The model is derived from the full 10 band model used by Ref. 14. We begin by summarising this full 10 band model before introducing the low energy 2 band model we use for the remainder of the paper.

1. Full pentalayer model

We describe the full model of R5G, see Ref. 14 for more details. Graphene has a lattice parameter a = 2.46Å and lattice vectors,

$$\mathbf{R}_1 = (a, 0) \tag{A1}$$

$$\mathbf{R}_2 = a\left(\frac{1}{2}, \frac{\sqrt{3}}{2}\right). \tag{A2}$$

The corresponding reciprocal lattice vectors are

$$G_1 = \frac{2\pi}{a} \left(1, -\frac{1}{\sqrt{3}} \right) \tag{A3}$$

$$G_2 = \frac{2\pi}{a} \left(0, \frac{2}{\sqrt{3}} \right). \tag{A4}$$

The high symmetry points of graphene are,

$$\boldsymbol{K}_{Gr} = \frac{2}{3}\boldsymbol{G}_1 + \frac{1}{3}\boldsymbol{G}_2 \tag{A5}$$

$$\mathbf{K}'_{Gr} = \frac{1}{3}\mathbf{G}_1 + \frac{2}{3}\mathbf{G}_2. \tag{A6}$$

We can write the Hamiltonian for R5G in layer space as,

$$h_{R5G}(\mathbf{k}) = \begin{bmatrix} h_0^{(0)} & h^{(1)} & h^{(2)} & 0 & 0\\ [h^{(1)}]^{\dagger} & h_1^{(0)} & h^{(1)} & h^{(2)} & 0\\ [h^{(2)}]^{\dagger} & [h^{(1)}]^{\dagger} & h_2^{(0)} & h^{(1)} & h^{(2)}\\ 0 & [h^{(2)}]^{\dagger} & [h^{(1)}]^{\dagger} & h_3^{(0)} & h^{(1)}\\ 0 & 0 & [h^{(2)}]^{\dagger} & [h^{(1)}]^{\dagger} & h_4^{(0)}, \end{bmatrix}$$
(A7)

where the rows and columns correspond to different layers of graphene. The $h_l^{(0)}$, $h^{(1)}$ and $h^{(2)}$ matrices are written in the basis of the graphene sublattice orbitals for each layer (l) of graphene in the pentalayer stack. These matrices are,

$$h_l^{(0)}(\mathbf{k}) = \begin{pmatrix} u_l & -t_0 f_{\mathbf{k}} \\ -t_0 \bar{f}_{\mathbf{k}} & u_l \end{pmatrix}, \tag{A8}$$

$$h^{(1)}(\mathbf{k}) = \begin{pmatrix} t_4 & t_3 \bar{f}_{\mathbf{k}} \\ t_1 \bar{f}_{\mathbf{k}} & t_4 f_{\mathbf{k}} \end{pmatrix},\tag{A9}$$

$$h^{(2)}(\mathbf{k}) = \begin{pmatrix} 0 & \frac{t_2}{2} \\ 0 & 0 \end{pmatrix}. \tag{A10}$$

We define.

$$f_{\mathbf{k}} = \sum_{i=0}^{2} e^{\mathrm{i}\mathbf{k}.\boldsymbol{\delta}_{i}},\tag{A11}$$

with δ_n defined as the vectors between nearest neighbour carbon atoms in each layer [14]. We use the hopping values $t_0 = 3.1 \,\text{eV}$, $t_1 = 380 \,\text{meV}$, $t_2 = -21 \,\text{meV}$, $t_3 = 290 \,\text{meV}$ and $t_4 = 141 \,\text{meV}$ [14, 25]. The applied electric field gives a layer dependent electric potential,

$$u_l = u_D l \tag{A12}$$

with the layer index l and the tunable displacement field u_D .

2. Low energy model

We now derive the low energy model of pentalayer rhombohedral graphene. For finite u_D there are two bands immediately above and below the Fermi energy at charge neutrality. These two bands are layer polarised around the K_{Gr} point. The band which is layer polarised to layer 1 has most of the wave function weight on the A sublattice whereas the layer 5 polarised band is on the B sublattice. The low energy physics, around K_{Gr} , can therefore be well described by a model solely in the subspace 1A, 5B (where we label the positions in the unit cell by the layer 1, 5 and the sublattice A, B). We rewrite the equation for the energy dispersion $\epsilon(k)$ as,

$$\begin{pmatrix} h(\mathbf{k})_{11} & h(\mathbf{k})_{12} \\ h(\mathbf{k})_{21} & h(\mathbf{k})_{22} \end{pmatrix} \begin{pmatrix} \mathbf{c}_1(\mathbf{k}) \\ \mathbf{c}_2(\mathbf{k}) \end{pmatrix} = \epsilon(\mathbf{k}) \begin{pmatrix} \mathbf{c}_1(\mathbf{k}) \\ \mathbf{c}_2(\mathbf{k}) \end{pmatrix}, \tag{A13}$$

where the matrix $h(\mathbf{k})_{11}$ represents the block of the full matrix $h(\mathbf{k})$ in the subspace $1A, 5B, h(\mathbf{k})_{22}$ is the high energy subspace $(i.e.\ 2B, ..., 5A)$, and $h(\mathbf{k})_{12}$ and $h(\mathbf{k})_{21}$ represents the coupling between the subspaces. The components of the Bloch function in each subspace are given by the functions $\mathbf{c}_1(\mathbf{k})$ and $\mathbf{c}_2(\mathbf{k})$. We wish to find a 2×2 effective Hamiltonian in the low energy subspace [33]. To do this we expand Eq. (A13) to give two relations,

$$\mathbf{c}_1(\mathbf{k}) = (\epsilon - h(\mathbf{k})_{11})^{-1} h(\mathbf{k})_{12} \mathbf{c}_2(\mathbf{k})$$
(A14)

$$\mathbf{c}_{2}(\mathbf{k}) = (\epsilon - h(\mathbf{k})_{22})^{-1}h(\mathbf{k})_{21}\mathbf{c}_{1}(\mathbf{k}). \tag{A15}$$

Combining these we obtain an equation for the wave function components in the low energy subspace $c_1(k)$,

$$[h_{11}(\mathbf{k}) + h_{12}(\mathbf{k})(h_{22}(\mathbf{k}) - \epsilon)^{-1}h_{21}(\mathbf{k}) - \epsilon]\mathbf{c}_1(\mathbf{k}) = 0.$$
(A16)

We expand to first order in energy ϵ and obtain the effective Hamiltonian, [33]

$$h_{\text{eff}}(\mathbf{k}) = \left\{ 1 - h(\mathbf{k})_{12} \left[h(\mathbf{k})_{22} \right]^{-2} h(\mathbf{k})_{21} \right\}^{-1} \\ \left\{ h(\mathbf{k})_{11} + h(\mathbf{k})_{12} \left[h(\mathbf{k})_{22} \right]^{-1} h(\mathbf{k})_{21} \right\}.$$
(A17)

We consider small momenta around the K_{Gr} valley of the R5G, and so we Taylor expand $h_{\text{eff}}(\mathbf{k})$ in powers of \mathbf{k} about K_{Gr} . For pentalayer rhombohedral graphene, the dominant off-diagonal terms in $h_{\text{eff}}(\mathbf{k})$ go as $\sim |\mathbf{k}|^5$ (as described in Ref. [18]). When we expand the diagonal elements to zeroth order in \mathbf{k} we also obtain a contribution from the applied displacement field u_D . We introduce a further correction beyond the model described in Ref. 18; the full model has a characteristic quadratic curvature which dominates at small momenta \mathbf{k} from the Dirac point K_{Gr} . We find that this effect can be captured in the low energy model by expanding the diagonal components to second order in momentum \mathbf{k} . This gives an effective hamiltonian in the low energy subspace which is,

$$h_{\text{eff}}(k_x, k_y) = \begin{pmatrix} 2u_D + \gamma_-(k_x^2 + k_y^2) & \frac{v_F^5}{t_0^4} (k_x - ik_y)^5 \\ \frac{v_F^5}{t_0^4} (k_x + ik_y)^5 & -2u_D + \gamma_+(k_x^2 + k_y^2) \end{pmatrix}.$$
(A18)

The $\gamma_{0/1}$ take a simple form if we assume small u_D (specifically $u_D < v_3/a \ll v_F/a$) and expand to first order in u_D ,

$$\gamma_{\pm} \approx \frac{2v_F v_4}{t_1} \pm \frac{u_D v_F^2}{t_1^2}.$$
(A19)

This simplified model predicts a sign change in the curvature of the higher-energy band at the K_{Gr} point at a displacement field of $u_D = \frac{2v_4t_1}{v_F} \sim 35 \,\mathrm{meV}$, while the band dispersion curvature at the K_{Gr} point of the lower-energy band remains unchanged for all $u_D \geq 0$. This behaviour in good agreement with results from the full model. Note that this curvature sign change is not captured in the simple model described in Ref. 18 so this model more accurately describes the low energy physics of R5G. A comparison between the dispersions of the full and simplified models for a representative parameter set is shown in the main text. As expected, the two models agree well at momenta close to K_{Gr} , with increasing deviation at larger momenta. Notably, the full model lacks inversion symmetry about the K_{Gr} point—i.e., it is not symmetric under $(k_x, k_y) \to (-k_x, -k_y)$ —unlike the low-energy approximation. This asymmetry arises from the inclusion of intra-layer hopping t_3 . When t_3 is neglected, the system possesses a unitary symmetry $U = \bigoplus_{l=0}^{N_l-1} (-1)^l \sigma_z$, obeying $Uh(\mathbf{k})U^{\dagger} = h(-\mathbf{k})$. This makes the spectrum symmetric about about the K_{Gr} . Since the low-energy 2 × 2 model does not include t_3 , it is symmetric about the K_{Gr} point. In addition to capturing the low energy dispersion, the low energy model derived above also captures the Berry curvature distribution of the full model (as the model without the quadratic correction does too [18]).

Appendix B: Moiré Hamiltonian

We study R5G between hBN layers *i.e.* hBN/R5G/hBN stacks. We use the same model as Ref. 14. The lattice mismatch between the hBN and the R5G leads to a moiré pattern. There are two sources of the lattice mismatch: firstly there is a lattice constant mismatch between hBN and graphene, $\epsilon = a_{\rm hBN}/a_{Gr} = 0.018$. Secondly we can rotate the hBN by some angle θ to change the moiré periodicity. We define a rotation matrix R_{θ} to describe rotation of the hBN graphene by angle θ with respect to the R5G. Similarly the matrix $M = (1 + \epsilon)I$ can be used to calculate the effects of the lattice constant mismatch. The moiré reciprocal lattice vectors are,

$$\boldsymbol{g}_i = [I - M^{-1}R_\theta]\boldsymbol{G}_i,\tag{B1}$$

for $j \in \{1, 2\}$ [14, 25]. In addition we define,

$$\mathbf{g}_3 = \mathbf{g}_1 + \mathbf{g}_2. \tag{B2}$$

The high symmetry points in the new moiré Brillouin zone are,

$$\gamma = K_{Gr} \tag{B3}$$

$$\kappa^+ = \gamma - \frac{1}{3}g_1 + \frac{1}{3}g_2 \tag{B4}$$

$$\kappa^- = \gamma - \frac{2}{3}\mathbf{g}_1 - \frac{1}{3}\mathbf{g}_2 \tag{B5}$$

$$\mu = \gamma - \frac{1}{2}g_1. \tag{B6}$$

We model the effect of the hBN layers as an effective potential acting on the outermost layers (l = 1, 5) of the R5G. This moiré potential can be written as,

$$H_V = \sum_{\substack{\mathbf{r} \\ l \in \{\text{top,btm}\}}} V_{\text{eff}}^l(\mathbf{r}) c_{\mathbf{r},l}^{\dagger} c_{\mathbf{r},l}, \tag{B7}$$

r goes over all unit cells and $c_{r,l}^{\dagger}$ creates an electron at position r and layer l. Since our effective Hamiltonian retains only the A sublattice in the bottom layer and the B sublattice in the top layer, we apply the moiré potential exclusively to these sites. The moiré potential has the moiré periodicity so we can write the potential as,

$$V_{\text{eff}}^{l}(\boldsymbol{r}) = \sum_{\substack{\eta \in \{1,-1\}\\j \in \{1,2,3\}}} V_{l,\eta\boldsymbol{g}_{j}} \exp\left[i\eta\boldsymbol{g}_{j} \cdot \boldsymbol{r}\right]$$
(B8)

Here, the sum runs over the first shell of moiré reciprocal lattice vectors around the first moiré BZ. This is known as the "first harmonic" approximation. We use values for the prefactors $V_{l,\eta g_j}$ introduced in Ref. [25] such that the potential can be expressed as,

$$V_{\text{eff}}^{l}(\mathbf{r}) = V_0 + V_1 \sum_{\substack{\eta \in \{1, -1\}\\ j \in \{1, 2.3\}}} \exp\left[i\eta \left(\mathbf{g}_j \cdot \mathbf{r} + \psi_{\xi} + \phi_l\right)\right]. \tag{B9}$$

There is a phase shift ψ_{ξ} which depends on the the stacking configuration, for example, the A sublattice of graphene may lie above either a boron atom ($\xi=0$) or a nitrogen atom ($\xi=1$), as described in Ref. [25] and this leads to differing phases for the effective potential. We use the values in Refs. [25] and restrict our study to the $\xi=0$ stacking for both the top and bottom layers, for which $\psi_{\xi}=223.5^{\circ}$. The additional phase factor ϕ_{l} is 0 for the bottom layer but for N_{l} layers of graphene, the top layer gains a phase $\phi_{l}=\frac{2\pi N_{l}}{3}$. This phase accounts for the relative shift in the moiré pattern that arises because, in a given unit cell, the B sublattice site in the top layer is not directly aligned above the A sublattice sites in the bottom layer [13]. Note that the moiré coupling does not couple the top and bottom layers. We use $V_{0}=28.9$ meV and $V_{1}=21.0$ meV following Refs. 14 and 25.

We rewrite the Hamiltonian in momentum space using,

$$c_{\boldsymbol{r},l}^{\dagger} = \frac{1}{L} \sum_{\boldsymbol{k}} e^{i\boldsymbol{k}\cdot\boldsymbol{r}} c_{\boldsymbol{k},l}^{\dagger}.$$
 (B10)

where the sum over k goes over all momenta in the R5G BZ and the system consists of L^2 unit cells. This gives,

$$H_V = \sum_{\substack{l, r, k, k' \\ j \in \{1, 2, 3\}}} \sum_{\substack{e^{i(k-k'+g_j) \cdot r} V_{l, \eta g_j} c_{k, l}^{\dagger} c_{k', l}} e^{i(k-k'+g_j) \cdot r} V_{l, \eta g_j} c_{k, l}^{\dagger} c_{k', l}.$$
(B11)

Performing the summation over r gives,

$$H_V = \sum_{\substack{l, \boldsymbol{k}, \boldsymbol{k}' \\ j \in \{1, 2, 3\}}} \sum_{\substack{\boldsymbol{k}, \boldsymbol{k}' - \eta \boldsymbol{g}_j \\ j \in \{1, 2, 3\}}} \delta_{\boldsymbol{k}, \boldsymbol{k}' - \eta \boldsymbol{g}_j} V_{l, \eta \boldsymbol{g}_j} c_{\boldsymbol{k}, l}^{\dagger} c_{\boldsymbol{k}', l}.$$
(B12)

We now express all momenta in terms of the momentum in the mBZ (k) and a moiré reciprocal lattice vector (Q) i.e. $c_{k,Q,l}^{\dagger} \equiv c_{k+Q,l}^{\dagger}$ we obtain,

$$H_{V} = \sum_{l} \sum_{\mathbf{k}} \sum_{\mathbf{Q}, \mathbf{Q}'} \sum_{\substack{\eta \in \{1, -1\} \\ j \in \{1, 2, 3\}}} (\delta_{\mathbf{Q}, \mathbf{Q}' - \eta \mathbf{g}_{j}} V_{l, \eta \mathbf{g}_{j}}) c_{\mathbf{k}, \mathbf{Q}, l}^{\dagger} c_{\mathbf{k}, \mathbf{Q}', l}.$$
(B13)

The sum over Q, Q' is over all moiré reciprocal lattice vectors, *i.e.* not restricted to the first ring about the mBZ. We obtain the full moire Hamiltonian,

$$H_{M} = H_{0} + H_{V} = \sum_{\boldsymbol{k} \in \text{mBZ}} \sum_{\boldsymbol{Q}, \boldsymbol{Q}'} \sum_{l,l'} h_{(\boldsymbol{Q},l),(\boldsymbol{Q}',l')}^{(m)}(\boldsymbol{k}) c_{\boldsymbol{k},\boldsymbol{Q},l}^{\dagger} c_{\boldsymbol{k},\boldsymbol{Q}',l'}, \tag{B14}$$

where,

$$h_{(\mathbf{Q},l),(\mathbf{Q}',l')}^{(m)}(\mathbf{k}) = \{ [h_{\text{eff}}(\mathbf{k}+\mathbf{Q})]_{l,l'} + V_0 \delta_{l,l'} \} \, \delta_{\mathbf{Q},\mathbf{Q}'} + \sum_{\substack{\eta \in \{1,-1\}\\j \in \{1,2,3\}}} (\delta_{\mathbf{Q},\mathbf{Q}'-\eta \mathbf{g}_j} V_1).$$
(B15)

Here the first term $h_{\rm eff}(\mathbf{k})$ represents the low energy R5G without the moiré coupling. The moiré system retains C_3 symmetry and so there are three high symmetry points γ , κ_+ and κ_- . To obtain a finite matrix size, we truncate the set of \mathbf{Q} vectors in the moiré Hamiltonian to those within a ring around the γ point with $|\mathbf{Q}| \leq 5[2\pi \cdot (a_{\rm moir\acute{e}})^{-1}]$, where $a_{\rm moir\acute{e}}$ is the moiré lattice parameter.

Appendix C: Phase diagram of non-interacting model

We plot the Chern numbers of the conduction and valence bands (e.g. see Fig. 4 in main text) as a function of applied field u_D and twist angle θ . The resulting phase diagrams are shown in Fig. 7. We see that both bands can have Chern numbers 0, 1 & 2 (mod 3). We choose to study excitons at the experimental angle $\theta = 0.77^{\circ}$ at the displacement fields $u_D = \pm 20 \text{ meV}$.

Appendix D: Exciton Hamiltonian

We calculate the exciton spectra and wave functions using the following method. We project the fully many-body Hamiltonian into the variational basis,

$$|\boldsymbol{p}, \boldsymbol{k}\rangle = c_{\boldsymbol{p}+\boldsymbol{k},c}^{\dagger} c_{\boldsymbol{k},v} |\text{GS}\rangle.$$
 (D1)

The total momentum of the above state is p, the relative momentum is k.

We project the full Hamiltonian onto the variational basis and calculate its matrix elements,

$$\langle \boldsymbol{p}, \boldsymbol{k} | \hat{H} | \boldsymbol{p}, \boldsymbol{k}' \rangle$$
. (D2)

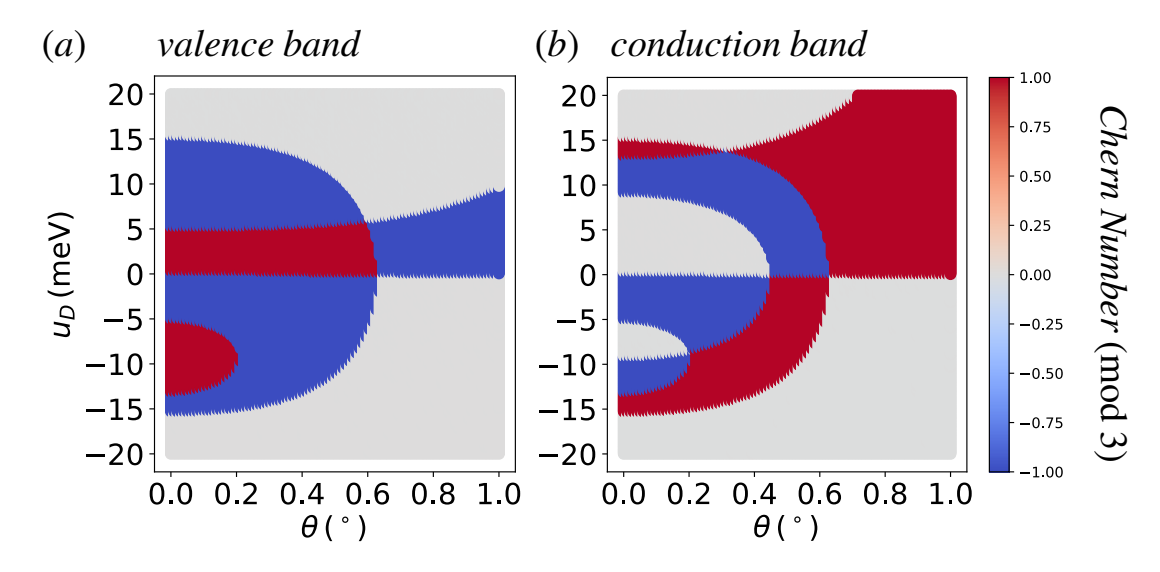


FIG. 7. Chern numbers (mod 3) of the valence and conduction bands as a function of the twist angle of the hBN with respect to the R5G and the applied potential u_D .

We have a contribution from the kinetic Hamiltonian [Eq. (B14)],

$$\langle \boldsymbol{p}, \boldsymbol{k} | \hat{H}_0 | \boldsymbol{p}, \boldsymbol{k}' \rangle = \delta_{\boldsymbol{k}, \boldsymbol{k}'} (E_{G.S.} - \epsilon_{\boldsymbol{k}, v} + \epsilon_{\boldsymbol{p} + \boldsymbol{k}, c}),$$
 (D3)

where $\epsilon_{\boldsymbol{p},c/v}$ are the single particle energies of the kinetic hamiltonian for the conduction/valence bands at momentum \boldsymbol{p} . The ground state energy is $E_{\text{G.S.}} = \sum_{\boldsymbol{k}} \epsilon_{\boldsymbol{k},v}$.

We also project the interaction term into this basis. We first derive the general form of the matrix elements before showing the results for the moiré Hamiltonian. We begin with the general form of a translationally-symmetric interaction Hamiltonian,

$$\hat{H}_{int} = \sum_{\mathbf{R}, \mathbf{R}', i, j} U_{\mathbf{R} - \mathbf{R}', i, j} \hat{n}_{\mathbf{R}, i} \hat{n}_{\mathbf{R}', j} \tag{D4}$$

where $\hat{n}_{R,i}$ is the number operator at unit cell R and i labels the sublattices. Now we write this in the momentum basis. First note that

$$c_{\mathbf{k},i}^{\dagger} = \frac{1}{\sqrt{V}} \sum_{\mathbf{R}} e^{i\mathbf{k}\cdot\mathbf{R}} c_{\mathbf{R},i}^{\dagger} \tag{D5}$$

$$c_{\mathbf{R},i}^{\dagger} = \frac{1}{\sqrt{V}} \sum_{\mathbf{R}} e^{-i\mathbf{k}\cdot\mathbf{R}} c_{\mathbf{k},i}^{\dagger}.$$
 (D6)

We rewrite the number operators as,

$$n_{\mathbf{R},i} = c_{\mathbf{R},i}^{\dagger} c_{\mathbf{R},i} \tag{D7}$$

$$= \frac{1}{V} \sum_{\mathbf{p},\mathbf{q}} e^{-i(\mathbf{p}-\mathbf{q}) \cdot \mathbf{R}} c_{\mathbf{p},i}^{\dagger} c_{\mathbf{q},i}. \tag{D8}$$

Equation D4 becomes,

$$\hat{H}_{\text{int}} = \sum_{\mathbf{R}, \mathbf{R}', i, j} \sum_{\mathbf{p}, \mathbf{q}, \mathbf{p}', \mathbf{q}'} \frac{1}{V^2} U_{\mathbf{R} - \mathbf{R}', ij} e^{-i(\mathbf{p} - \mathbf{q}) \cdot \mathbf{R} - i(\mathbf{p}' - \mathbf{q}') \cdot \mathbf{R}'} c_{\mathbf{p}i}^{\dagger} c_{\mathbf{q}i} c_{\mathbf{p}'j}^{\dagger} c_{\mathbf{q}'j}$$
(D9)

$$= \sum_{\mathbf{R},\mathbf{R}',i,j} \sum_{\mathbf{p},\mathbf{q},\mathbf{p}',\mathbf{q}'} \frac{1}{V^2} U_{\mathbf{R},ij} e^{-i(\mathbf{p}-\mathbf{q})R - i(\mathbf{p}'-\mathbf{q}' + \mathbf{p}' - \mathbf{q}') \cdot \mathbf{R}'} c_{\mathbf{p}i}^{\dagger} c_{\mathbf{q}i} c_{\mathbf{p}'j}^{\dagger} c_{\mathbf{q}'j}, \tag{D10}$$

where we set $R - R' \to R$. This can be further simplified by performing the sum over R' and q' to give

$$\hat{H}_{\text{int}} = \frac{1}{V} \sum_{\mathbf{R},i,j} \sum_{\mathbf{pqp'}} U_{\mathbf{R},ij} e^{-i(\mathbf{p}-\mathbf{q}) \cdot \mathbf{R}} c_{\mathbf{p},i}^{\dagger} c_{\mathbf{q},i} c_{\mathbf{p'},j}^{\dagger} c_{\mathbf{p}-\mathbf{q}+\mathbf{p'},j}. \tag{D11}$$

Let $U_{\mathbf{p},ij} = \frac{1}{V} \sum_{\mathbf{R}} U_{\mathbf{R},ij} e^{-i\mathbf{p}\cdot\mathbf{R}},$

$$\hat{H}_{\text{int}} = \sum_{\boldsymbol{p} \boldsymbol{q} \boldsymbol{q}' i j} U_{\boldsymbol{p}, i j} c_{\boldsymbol{p} + \boldsymbol{q}, i}^{\dagger} c_{\boldsymbol{q}, i} c_{\boldsymbol{q}', j}^{\dagger} c_{\boldsymbol{p} + \boldsymbol{q}', j}. \tag{D12}$$

To calculate the matrix elements

$$\langle \boldsymbol{p}, \boldsymbol{k} | \hat{H}_{\text{int}} | \boldsymbol{p}, \boldsymbol{k}' \rangle$$
 (D13)

we express the interaction Hamiltonian in the band basis. The Bloch function for band α , is $u_i^{k,\alpha}$ meaning that,

$$c_{\mathbf{k},\alpha}^{\dagger} = \sum u_i^{\mathbf{k},\alpha} c_{\mathbf{k},i}^{\dagger} \tag{D14}$$

$$c_{\mathbf{k},\alpha} = \sum_{i} \bar{u}_{i}^{\mathbf{k},\alpha} c_{\mathbf{k},i} \tag{D15}$$

where i sums over the sub-lattices, and $\alpha \in \{c, v\}$. We use the notation $\bar{u}_i^{k,\alpha} = (u_i^{k,\alpha})^*$. Plugging this relation into equation D12 we obtain

$$\hat{H}_{\text{int}} = \sum_{\boldsymbol{p}\boldsymbol{q}\boldsymbol{q}'ij} U_{\boldsymbol{p},ij} c_{\boldsymbol{p}+\boldsymbol{q},i}^{\dagger} c_{\boldsymbol{q},i} c_{\boldsymbol{q}',j}^{\dagger} c_{\boldsymbol{p}+\boldsymbol{q}',j}$$
(D16)

$$= \sum_{\boldsymbol{p}\boldsymbol{q}\boldsymbol{q}'ij\alpha\alpha'\beta\beta'} U_{\boldsymbol{p},ij} \bar{u}_{i}^{\boldsymbol{p}+\boldsymbol{q},\alpha} u_{i}^{\boldsymbol{q}\alpha'} \bar{u}_{j}^{\boldsymbol{q}',\beta} u_{j}^{\boldsymbol{p}+\boldsymbol{q}'\beta'} c_{\boldsymbol{p}+\boldsymbol{q},\alpha}^{\dagger} c_{\boldsymbol{q},\alpha'} c_{\boldsymbol{q}',\beta}^{\dagger} c_{\boldsymbol{p}+\boldsymbol{q}',\beta'}. \tag{D17}$$

Defining $U_{\alpha\alpha'\beta\beta'}^{m{p}qm{q}'}=\sum_{ij}(U_{m{p},ij}\bar{u}_i^{m{p}+m{q},\alpha}u_i^{m{q}\alpha'}\bar{u}_j^{m{q}',\beta}u_j^{m{p}+m{q}'\beta'})$ we can write

$$\hat{H}_{\text{int}} = \sum_{\boldsymbol{p}\boldsymbol{q}\boldsymbol{q}'\alpha\alpha'\beta\beta'} U_{\alpha\alpha'\beta\beta'}^{\boldsymbol{p}\boldsymbol{q}\boldsymbol{q}'} c_{\boldsymbol{p}+\boldsymbol{q},\alpha}^{\dagger} c_{\boldsymbol{q},\alpha'} c_{\boldsymbol{q}',\beta}^{\dagger} c_{\boldsymbol{p}+\boldsymbol{q}',\beta'}. \tag{D18}$$

The matrix elements are,

$$\langle \boldsymbol{p}, \boldsymbol{k} | \hat{H}_{\text{int}} | \boldsymbol{p}, \boldsymbol{k}' \rangle = \sum_{\boldsymbol{l} \boldsymbol{q} \boldsymbol{q}' \alpha \alpha' \beta \beta'} U_{\alpha \alpha' \beta \beta'}^{\boldsymbol{l} \boldsymbol{q} \boldsymbol{q}'} \langle \text{GS} | c_{\boldsymbol{k}, v}^{\dagger} c_{\boldsymbol{p} + \boldsymbol{k}, c} c_{\boldsymbol{l} + \boldsymbol{q}, \alpha}^{\dagger} c_{\boldsymbol{q}, \alpha'} c_{\boldsymbol{q}', \beta}^{\dagger} c_{\boldsymbol{l} + \boldsymbol{q}', \beta'} c_{\boldsymbol{p} + \boldsymbol{k}', c}^{\dagger} c_{\boldsymbol{k}', v} | \text{GS} \rangle. \tag{D19}$$

Wick's theorem can be used to simplify the expectation value,

$$\langle GS | c_{\mathbf{k},v}^{\dagger} c_{\mathbf{p}+\mathbf{k},c} c_{\mathbf{l}+\mathbf{q},\alpha}^{\dagger} c_{\mathbf{q},\alpha'} c_{\mathbf{q}',\beta}^{\dagger} c_{\mathbf{l}+\mathbf{q}',\beta'} c_{\mathbf{p}+\mathbf{k}',c}^{\dagger} c_{\mathbf{k}',v} | GS \rangle.$$
 (D20)

For readability we simplify the notation to

$$\mu^{\dagger} = c_{\mathbf{k},v}^{\dagger},\tag{D21}$$

$$\nu = c_{\boldsymbol{p}+\boldsymbol{k},c},\tag{D22}$$

$$\zeta^{\dagger} = c_{l+q,\alpha}^{\dagger},\tag{D23}$$

$$\sigma = c_{\mathbf{q},\alpha'},\tag{D24}$$

$$\chi^{\dagger} = c_{\mathbf{q}',\beta}^{\dagger},\tag{D25}$$

$$\gamma = c_{l+q',\beta'},$$

$$\lambda^{\dagger} = c_{p+k',c}^{\dagger},$$
(D26)

$$\xi = c_{\mathbf{k}', \mathbf{v}}.\tag{D28}$$

The expectation value becomes

$$\langle \mu^{\dagger} \nu \zeta^{\dagger} \sigma \chi^{\dagger} \gamma \lambda^{\dagger} \xi \rangle \tag{D29}$$

This can be expanded using Wick's theorem as

$$\langle \mu^{\dagger} \nu \zeta^{\dagger} \sigma \chi^{\dagger} \gamma \lambda^{\dagger} \xi \rangle = \langle \mu^{\dagger} \sigma \rangle (\langle \nu \zeta^{\dagger} \rangle \langle \chi^{\dagger} \xi \rangle \langle \gamma \lambda^{\dagger} \rangle - \langle \nu \chi^{\dagger} \rangle \langle \zeta^{\dagger} \xi \rangle \langle \gamma \lambda^{\dagger} \rangle - \langle \nu \lambda^{\dagger} \rangle (\langle \zeta^{\dagger} \xi \rangle \langle \chi^{\dagger} \gamma \rangle - \langle \zeta^{\dagger} \gamma \rangle \langle \chi^{\dagger} \xi \rangle))$$

$$+ \langle \mu^{\dagger} \gamma \rangle (-\langle \nu \zeta^{\dagger} \rangle \langle \sigma \lambda^{\dagger} \rangle \langle \chi^{\dagger} \zeta \rangle + \langle \nu \chi^{\dagger} \rangle \langle \zeta^{\dagger} \xi \rangle \langle \sigma \lambda^{\dagger} \rangle - \langle \nu \lambda^{\dagger} \rangle (\langle \zeta^{\dagger} \sigma \rangle \langle \chi^{\dagger} \xi \rangle + \langle \zeta^{\dagger} \xi \rangle \langle \sigma \chi^{\dagger} \rangle))$$

$$+ \langle \mu^{\dagger} \xi \rangle (\langle \nu \zeta^{\dagger} \rangle (\langle \sigma \chi^{\dagger} \rangle \langle \gamma \lambda^{\dagger} \rangle + \langle \sigma \lambda^{\dagger} \rangle \langle \chi^{\dagger} \gamma \rangle) + \langle \nu \chi^{\dagger} \rangle (\langle \zeta^{\dagger} \sigma \rangle \langle \chi^{\dagger} \gamma \rangle + \langle \zeta^{\dagger} \gamma \rangle \langle \sigma \chi^{\dagger} \rangle)). \quad (D30)$$

We simplify the expression using the values of the two particle correlators. After performing the sum in equation D19 we obtain,

$$\langle \boldsymbol{p}, \boldsymbol{k} | \hat{H}_{\text{int}} | \boldsymbol{p}, \boldsymbol{k}' \rangle = U_{cvvc}^{\boldsymbol{p}, \boldsymbol{k}, \boldsymbol{k}'} + U_{vccv}^{-\boldsymbol{p}, \boldsymbol{p} + \boldsymbol{k}', \boldsymbol{p} + \boldsymbol{k}} - U_{vvcc}^{\boldsymbol{k}' - \boldsymbol{k}, \boldsymbol{k}, \boldsymbol{p} + \boldsymbol{k}} - U_{ccvv}^{\boldsymbol{k} - \boldsymbol{k}', \boldsymbol{p} + \boldsymbol{k}', \boldsymbol{k}'} + \delta_{\boldsymbol{k}, \boldsymbol{k}'} \sum_{\boldsymbol{q}} (U_{vvvv}^{\boldsymbol{q}, \boldsymbol{k}, \boldsymbol{k}} - U_{vvvv}^{\boldsymbol{0}, \boldsymbol{q}, \boldsymbol{q}} - U_{vcvv}^{\boldsymbol{0}, \boldsymbol{q}, \boldsymbol{k} - \boldsymbol{q}} + U_{vccv}^{\boldsymbol{q}, \boldsymbol{k} - \boldsymbol{q}, \boldsymbol{q}, \boldsymbol{q}} + U_{ccvc}^{\boldsymbol{0}, \boldsymbol{p} + \boldsymbol{k}, \boldsymbol{q}} + U_{vvcc}^{\boldsymbol{0}, \boldsymbol{p} + \boldsymbol{k}, \boldsymbol{q}} + U_{vvcc}^{\boldsymbol{0}, \boldsymbol{p} + \boldsymbol{k}, \boldsymbol{q}} + U_{vvcc}^{\boldsymbol{0}, \boldsymbol{q}, \boldsymbol{p} + \boldsymbol{k}} - U_{vccv}^{\boldsymbol{q}, \boldsymbol{p} + \boldsymbol{k}, \boldsymbol{p} + \boldsymbol{k}}) + \delta_{\boldsymbol{k}, \boldsymbol{k}'} \sum_{\boldsymbol{q}, \boldsymbol{q}'} (U_{vvvv}^{\boldsymbol{0}, \boldsymbol{q}, \boldsymbol{q}'} + U_{vccv}^{\boldsymbol{q}, \boldsymbol{q}', \boldsymbol{q}'}) \quad (D31)$$

Finally we note that the final term is equal to the shift of the ground state energy due to the interaction i.e.

$$\langle GS|H_{\text{int}}|GS\rangle = \sum_{\boldsymbol{q},\boldsymbol{q'}} (U_{vvvv}^{\boldsymbol{0},\boldsymbol{q},\boldsymbol{q'}} + U_{vccv}^{\boldsymbol{q},\boldsymbol{q'},\boldsymbol{q'}}). \tag{D32}$$

Therefore to find the exciton spectrum compared to the modified ground state energy, we subtract this term from the exciton Hamiltonian.

For a moiré Hamiltonian [e.g. of the form Eq. (B15)] the U matrices become,

$$U_{\alpha,\alpha',\beta,\beta'}^{\boldsymbol{p},\boldsymbol{k},\boldsymbol{k}'} = \sum_{\boldsymbol{Q}} V(\boldsymbol{p} + \boldsymbol{Q}) \left\langle u_{\boldsymbol{p}+\boldsymbol{k}+\boldsymbol{Q}}^{\alpha} \middle| u_{\boldsymbol{p}'}^{\alpha'} \right\rangle \left\langle u_{\boldsymbol{p}'}^{\beta} \middle| u_{\boldsymbol{p}+\boldsymbol{k}'+\boldsymbol{Q}}^{\beta'} \right\rangle ., \tag{D33}$$

where $|u_{\mathbf{p}}^{\alpha}\rangle$ is the eigenstate of the moiré Hamiltonian [Eq. (B15)] with momentum \mathbf{p} and for band $\alpha \in \{c, v\}$. The interactions are modelled as a double-gated Coulomb potential as in Ref. 14,

$$V(\mathbf{p}) = \frac{V_0 \tanh(|\mathbf{p}|d)}{|\mathbf{p}|},\tag{D34}$$

where d is the gate distance. We set $d=250\,\text{Å}$ [14] for the following calculations. The interaction strength $V_0=\frac{2\pi}{\epsilon_0\epsilon_r}$ depends on the relative permittivity ϵ_r , for which we use $\epsilon_r=6$. Note that the expression is in Gaussian units.

Appendix E: Exciton Wannier states

$$\frac{u_D \quad \lambda_{\gamma}^{\text{exc}} \lambda_{\kappa_{+}}^{\text{exc}} \boldsymbol{s}_{\text{exc}}}{20 \text{ meV} \quad \omega \quad 1 \quad \omega^* \quad 1c} \\ -20 \text{ meV} \quad \omega^* \quad 1 \quad \omega \quad 1b}$$

TABLE II. C_3 eigenvalues of the exciton wave function at high-symmetry points in the Brillouin zone for two different parameter choices. The exciton Wannier centre s_{exc} is stated in terms of the Wyckoff positions (see Fig. 8b).

We now use symmetry indicators to calculate the exciton Wannier centres. We label the exciton eigenstates in the exciton band of interest as $|\psi^p\rangle$. The maximally localised exciton Wannier states then take the form,

$$|W^{\mathbf{R}}\rangle = \frac{1}{\sqrt{V}} \sum_{\mathbf{p}} e^{-i\mathbf{p} \cdot \mathbf{R}} e^{i\phi(\mathbf{p})} |\psi^{\mathbf{p}}\rangle$$
 (E1)

where $e^{i\phi(\mathbf{p})}$ is a gauge transformation that maximally localises the exciton Wannier state [20, 21]. The C_3 eigenvalues of the exciton bands are shown in Tab II. Since the exciton band is trivial, the exciton Wannier states are exponentially localised. The C_3 symmetry then requires that the exciton Wannier centres sit at one of the maximal Wyckoff positions (1a, 1b, 1c in Fig. 8b). We calculate the C_3 eigenvalues we expect for exciton Wannier states localised at each of these locations.

1. Wyckoff position: 1a

The Wyckoff position 1a lies at the centre of the moiré unit cell. We wish to determine the relationship between the exciton Wannier centre and the exciton C_3 eigenvalues. We first express our exciton wave function in terms of

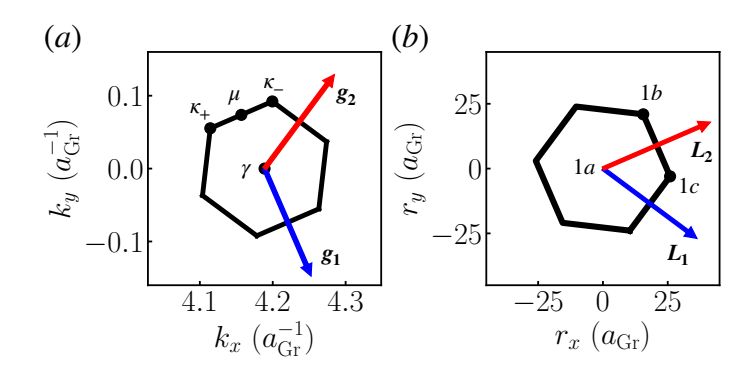


FIG. 8. Panel (a) is the mBZ of hBN/R5G/hBN for $\theta = 0.77^{\circ}$, moiré reciprocal lattice vectors $\mathbf{g_1}$, $\mathbf{g_2}$, and high symmetry points $\boldsymbol{\gamma}$, $\boldsymbol{\kappa_+}$, $\boldsymbol{\kappa_-}$ and $\boldsymbol{\mu}$. The real space unit cell [panel (b)] shows the lattice vectors $\boldsymbol{L_1}$, $\boldsymbol{L_2}$ and maximal Wyckoff positions 1a, 1b, 1c.

the maximally localised Wannier functions,

$$|\psi^{\mathbf{p}}\rangle = \frac{1}{\sqrt{V}} \sum_{\mathbf{p}} e^{i\mathbf{p} \cdot \mathbf{R}} |W^{\mathbf{R}}\rangle.$$
 (E2)

Next we consider how the C_3 operator acts on this wave function. The C_3 operator rotates real space positions by $2\pi/3$ about the 1a Wyckoff position within the $\mathbf{R} = 0$ unit cell. Therefore, under C_3 , the exciton Wannier state for unit cell \mathbf{R} is mapped to unit cell $U_{C_3}\mathbf{R}$ (the U_{C_3} operator rotates real space positions by $2\pi/3$). Applying \hat{C}_3 to the exciton wave function gives,

$$\hat{C}_3 |\psi^{\mathbf{p}}\rangle = \frac{1}{\sqrt{V}} \sum_{\mathbf{R}} e^{i\mathbf{p} \cdot \mathbf{R}} \hat{C}_3 |W^{\mathbf{R}}\rangle$$
 (E3)

$$= \lambda_W \frac{1}{\sqrt{V}} \sum_{\mathbf{R}} e^{i\mathbf{p} \cdot \mathbf{R}} |W^{\hat{U}_{C_3} \mathbf{R}}\rangle$$
 (E4)

$$= \lambda_W \frac{1}{\sqrt{V}} \sum_{\mathbf{R}} e^{i\mathbf{p} \cdot \hat{U}_{C_3}^{-1} \mathbf{R}} |W^{\mathbf{R}}\rangle$$
 (E5)

$$= \lambda_W \frac{1}{\sqrt{V}} \sum_{\mathbf{R}} e^{i\hat{U}_{C_3} \mathbf{p} \cdot \mathbf{R}} |W^{\mathbf{R}}\rangle, \qquad (E6)$$

where λ_W is a phase such that $\hat{C}_3 |W^{\mathbf{R}}\rangle = \lambda_W |W^{U_{C_3}\mathbf{R}}\rangle$. Since $[\hat{C}_3]^3$ is the identity therefore $\lambda_W \in \{1, \omega, \omega^*\}$. At the high symmetry points $\tilde{\mathbf{p}} \in \{\gamma, \kappa_+, \kappa_-\}$ (see Fig. 8) the exciton wave function is an eigenfunction of the \hat{C}_3 operator,

$$\hat{C}_3 |\psi^{\tilde{p}}\rangle = \lambda_W \frac{1}{\sqrt{V}} \sum_{R} e^{i\hat{U}_{C_3} \tilde{p} \cdot R} |W^R\rangle$$
 (E7)

$$= \lambda_W \frac{1}{\sqrt{V}} \sum_{\mathbf{R}} e^{i\mathbf{p} \cdot \mathbf{R}} |W^{\mathbf{R}}\rangle \tag{E8}$$

$$= \lambda_W |\psi^{\tilde{p}}\rangle. \tag{E9}$$

We see therefore that, when the exciton Wannier centres are at the 1a Wyckoff position, the C_3 eigenvalues are the same at all high symmetry points (and equal to λ_W). This is not true for either of the bands in Tab II and so their exciton Wannier centres are not at the 1a Wyckoff position.

2. Wyckoff position: 1b

We now find the symmetry eigenvalues of the exciton wave function if the exciton Wannier states sit at Wyckoff position 1b (Fig 8). The \hat{C}_3 operator rotates about the 1a Wyckoff position. Therefore, when the exciton Wannier state is centred at 1b, the exciton Wannier centre is transformed $\mathbf{R} \to \hat{U}_{C_3} \mathbf{R} - \mathbf{L}_2$ under the action of \hat{C}_3 (see Fig. 8b).

We consider the action of the C_3 operator on the exciton wave function,

$$\hat{C}_3 |\psi^{\mathbf{p}}\rangle = \frac{1}{\sqrt{V}} \sum_{\mathbf{R}} e^{i\mathbf{p} \cdot \mathbf{R}} \hat{C}_3 |W^{\mathbf{R}}\rangle$$
 (E10)

$$= \lambda_W \frac{1}{\sqrt{V}} \sum_{\mathbf{R}} e^{i\mathbf{p} \cdot \mathbf{R}} |W^{\hat{U}_{C_3} \mathbf{R} - \mathbf{L}_2}\rangle$$
 (E11)

$$= \lambda_W \frac{1}{\sqrt{V}} \sum_{\mathbf{R}} e^{i\mathbf{p} \cdot \hat{U}_{C_3}^{-1}(\mathbf{R} + \mathbf{L}_2)} |W^{\mathbf{R}}\rangle$$
 (E12)

$$= \lambda_W \frac{1}{\sqrt{V}} \sum_{\mathbf{R}} e^{i\hat{U}_{C_3} \mathbf{p} \cdot (\mathbf{R} + \mathbf{L}_2)} |W^{\mathbf{R}}\rangle.$$
 (E13)

Hence at the high symmetry points \tilde{p} ,

$$\hat{C}_3 |\psi^{\tilde{p}}\rangle = \lambda_W \frac{1}{\sqrt{V}} \sum_{\mathbf{R}} e^{i\tilde{p}\cdot(\mathbf{R} + \mathbf{L}_2)} |W^{\mathbf{R}}\rangle$$
(E14)

$$= \left(\lambda_W e^{i\tilde{\mathbf{p}} \cdot \mathbf{L}_2}\right) |\psi^{\tilde{\mathbf{p}}}\rangle. \tag{E15}$$

The C_3 eigenvalues at the high symmetry points are therefore,

$$\lambda_{C_3}(\tilde{\mathbf{p}}) = \lambda_W e^{\mathrm{i}\tilde{\mathbf{p}} \cdot \mathbf{L}_2}. \tag{E16}$$

Using $\omega = e^{-i\frac{2\pi}{3}}$ we can write the C_3 eigenvalues of the exciton wave function at the high symmetry points as $\lambda_{C_3}(\gamma) = \lambda_W$, $\lambda_{C_3}(\kappa_+) = \lambda_W \omega$ and $\lambda_{C_3}(\kappa_-) = \lambda_W \omega^*$. For $\lambda_W = \omega^*$ we see that this gives identical symmetry indicators to those shown for the excitons at $u_D = -20$ meV (see Tab. II). Therefore the exciton Wannier centres at $u_D = -20$ meV are at the 1b Wyckoff position.

3. Wyckoff position: 1c

The same method can be used to calculate the symmetry eigenvalues for exciton Wannier states that sit at the 1c Wyckoff position. Here we find that under C_3 the exciton Wannier state at unit cell R transforms to $\hat{U}_{C_3}R - L_1$. The symmetry eigenvalues therefore are,

$$\lambda_{C_3}(\tilde{\boldsymbol{p}}) = \lambda_W e^{\mathrm{i}\tilde{\boldsymbol{p}}\cdot\boldsymbol{L}_1}.\tag{E17}$$

We find that $\lambda_{C_3}(\gamma) = \lambda_W$, $\lambda_{C_3}(\kappa_+) = \lambda_W \omega^*$ and $\lambda_{C_3}(\kappa_-) = \lambda_W \omega$. For $\lambda_W = \omega$ this gives the symmetry indicators we found for the exciton band at displacement field $u_D = 20 \text{ meV}$ (see Tab. II). Therefore the exciton Wannier states at this displacement field are centred at the Wyckoff position 1c.

Appendix F: Exciton Berry curvature

In Ref. 21 we derived two exciton Wilson loops which relate to the projection of the electron and hole position operator into the exciton band. For 1D systems we obtain the two exciton Wilson loops for the conduction (c) and valence bands (v) respectively,

$$W_{\text{exc},c} = \prod_{p} \left[\sum_{k} \bar{\phi}_{k-p}^{p+\Delta} \phi_{k-p}^{p} \left\langle u_{k+\Delta,c} | u_{k,c} \right\rangle \right]$$
 (F1)

$$W_{\text{exc},v} = \prod_{p} \left[\sum_{k} \bar{\phi}_{k}^{p+\Delta} \phi_{k+\Delta}^{p} \langle u_{k+\Delta,v} | u_{k,v} \rangle \right].$$
 (F2)

with $\Delta = 2\pi/L$ for system size L. We note that these can both be written as a product of projectors,

$$W_{\text{exc},c/v} = \langle \mathcal{U}_{p_1}^{\text{exc},c/v} | \lim_{R \to \infty} \prod_{i=R}^{2} |\mathcal{U}_{p_i}^{\text{exc},c/v} \rangle \langle \mathcal{U}_{p_i}^{\text{exc},c/v} | |\mathcal{U}_{p_1}^{\text{exc},c/v} \rangle$$
(F3)

using,

$$|\mathcal{U}_{p}^{\mathrm{exc},c}\rangle = \sum_{k} \phi_{k}^{p} |k\rangle \otimes |u_{p+k,c}\rangle \otimes |\bar{u}_{k,v}\rangle$$
 (F4)

$$|\mathcal{U}_{p}^{\mathrm{exc},v}\rangle = \sum_{k} \phi_{k}^{p} |p+k\rangle \otimes |u_{p+k,c}\rangle \otimes |\bar{u}_{k,v}\rangle.$$
 (F5)

See Ref. 21 for details of the derivations.

Following the method introduced by Ref. 29 we can use these Wilson loop expressions to construct expressions for the flux through loops in the BZ. We consider the exciton wave functions which we have calculated on a grid with spacing d_{μ} in direction μ . We can define the link variables,

$$U_{\mu,c/v}(\mathbf{k}) = \frac{\langle \mathcal{U}^{\text{exc},c/v}(\mathbf{k}) | \mathcal{U}^{\text{exc},c/v}(\mathbf{k} + \mathbf{d}_{\mu}) \rangle}{|\langle \mathcal{U}^{\text{exc},c/v}(\mathbf{k}) | \mathcal{U}^{\text{exc},c/v}(\mathbf{k} + \mathbf{d}_{\mu}) \rangle|}.$$
 (F6)

We then calculate the lattice field strength,

$$F_{c/v}(\mathbf{k}) = -i \ln \left[U_{1,c/v}(\mathbf{k} + \mathbf{d}_1) U_{2,c/v}(\mathbf{k} + \mathbf{d}_2) U_{1,c/v}(\mathbf{k})^{-1} U_{2,c/v}(\mathbf{k})^{-1} \right]. \tag{F7}$$

For small $|d_{\mu}|$, $F_{c/v}(\mathbf{k})$ is proportional to the Berry curvature [29] and the Chern number of the band can be calculated as,

$$C = \frac{1}{2\pi} \sum_{\mathbf{k}} F_{c/v}(\mathbf{k}). \tag{F8}$$

This gives us a method to calculate the exciton Berry curvature without having to first find a smooth gauge. We have two expressions for the Berry curvature but for the system studied in this paper they both give similar Berry curvature distributions. In addition, they both integrate to the same value and so give the same Chern number. In the main text we therefore only plot one of the possible Berry curvature plots - that calculated using $|\mathcal{U}_p^{\text{exc},c}\rangle$.